MOLECULAR PHYSICS

Complex formation dynamics in a single-molecule electronic device

Huimin Wen,[1]* Wengang Li,[2]* Jiewei Chen,[1] Gen He,[1] Longhua Li,[3] Mark A. Olson,[2] Andrew C.-H. Sue,[2,4]† J. Fraser Stoddart,[2,4]† Xuefeng Guo[1,5]†

Single-molecule electronic devices offer unique opportunities to investigate the properties of individual molecules that are not accessible in conventional ensemble experiments. However, these investigations remain challenging because they require (i) highly precise device fabrication to incorporate single molecules and (ii) sufficient time resolution to be able to make fast molecular dynamic measurements. We demonstrate a graphene-molecule single-molecule junction that is capable of probing the thermodynamic and kinetic parameters of a host-guest complex. By covalently integrating a conjugated molecular wire with a pendent crown ether into graphene point contacts, we can transduce the physical [2]pseudorotaxane (de)formation processes between the electron-rich crown ether and a dicationic guest into real-time electrical signals. The conductance of the single-molecule junction reveals two-level fluctuations that are highly dependent on temperature and solvent environments, affording a non-destructive means of quantitatively determining the binding and rate constants, as well as the activation energies, for host-guest complexes. The thermodynamic processes reveal the host-guest binding to be enthalpy-driven and are consistent with conventional ^{1}H nuclear magnetic resonance titration experiments. This electronic device opens up a new route to developing single-molecule dynamics investigations with microsecond resolution for a broad range of chemical and biochemical applications.

INTRODUCTION

Since the inception of the donor-σ-acceptor molecular rectifier model in 1974 (*1*), molecular-level electronic devices have both experimentally and theoretically exhibited rapid growth (*2*–*7*). These advances demonstrate that the science of molecular electronics has become a multidisciplinary arena in which scientists can explore new fundamental concepts, starting from simple descriptions of charge transport and branching out in the direction of applications, including conductance switching (*8*), rectification (*5*, *9*), quantum interference effects (*10*, *11*), electroluminescence (*12*), thermoelectrics (*13*), molecular spintronics (*14*), biosensing (*15*), and memory devices (*16*). In combination with the abundant diversity of rationally designed molecules, the establishment of functional molecular circuits not only boosts the development of both device fabrication techniques and fundamental understanding of novel quantum effects, but also foresees new breakthroughs in the discovery of physical phenomena at the single-event or single-molecule level that are not accessible in ensemble experiments. Several previous investigations have focused on single-molecule electrical measurements of biomolecular interactions using nanowires (*17*, *18*), nanotubes (*19*–*21*), mechanical cantilevers (*22*), nanopores (*23*), and scanning tunneling microscope break junctions (*24*).

Among different molecular transport junctions (*25*–*30*), carbon electrode–molecule single-molecule junctions (CEM-SMJs), where carbon nanomaterials, such as single-walled carbon nanotubes (*31*) and graphene (*32*, *33*), are used as point contacts, are particularly attractive. This is because of (i) the unique properties of carbon electrodes (especially graphene), (ii) the ease of device fabrication, and (iii) the device reproducibility and stability. These CEM-SMJs hold great promise when it comes to realizing functional molecular devices that can convert intermolecular interactions or molecular behaviors, such as DNA hybridization, deoxyribozyme cleavage, DNA-protein interactions, and conformationally induced switching, into tangible electrical signals stemming from single-molecule recognition (*15*, *20*, *21*), thus rendering CEM-SMJs a reliable molecular electronics platform for practical applications (*6*). In this investigation, we demonstrate the capability of a graphene-molecule SMJ to probe the thermodynamic and kinetic parameters of single-event noncovalent bonding interactions between a crown ether and an electron-deficient guest. Among the early synthetic host-guest systems, the binding between crown ethers and cationic guests has been well studied by ultraviolet-visible spectroscopy (*34*–*36*), isothermal titration calorimetry (*37*), and nuclear magnetic resonance (NMR) titration protocols (*38*, *39*). These techniques are snapshots of the average behavior of molecular ensembles in solution at the micromolar/nanomolar level. By contrast, the CEM-SMJ approach takes advantage of the ultrasensitive single-molecule conductance, which can be modulated by the (de)complexation between the host situated in an SMJ and cationic guest molecules in solution, to transduce intermolecular interactions into electrical current signals with high bandwidth and signal-to-noise ratios. These results open up unique opportunities to study the stochastic and dynamic nature of molecular recognition processes in both chemical and biological systems with significant advantages, such as simple fabrication, low cost, no fluorescent labeling/bleaching problems, and direct real-time measurements at single-molecule sensitivity levels.

[1]Beijing National Laboratory for Molecular Sciences, State Key Laboratory for Structural Chemistry of Unstable and Stable Species, College of Chemistry and Molecular Engineering, Peking University, Beijing 100871, China. [2]Institute for Molecular Design and Synthesis, School of Pharmaceutical Science and Technology, Tianjin University, Tianjin 300072, China. [3]Scientific Research Academy, Jiangsu University, Zhenjiang 212013, China. [4]Department of Chemistry, Northwestern University, Evanston, IL 60208–3113, USA. [5]Department of Materials Science and Engineering, College of Engineering, Peking University, Beijing 100871, China.
*These authors contributed equally to this work.
†Corresponding author. Email: guoxf@pku.edu.cn (X.G.); andrew.sue@tju.edu.cn (A.C.-H.S.); stoddart@northwestern.edu (J.F.S.)

RESULTS AND DISCUSSION

Device fabrication and solid-state electrical characterization

Single-layered graphene was prepared on copper foils by a chemical vapor deposition process and transferred onto silicon wafers with a

300-nm layer of thermally grown silicon oxide (SiO_2) on the surface (fig. S1). Then, metal electrode arrays (8 nm/60 nm, Cr/Au) were patterned through photolithography and thermal evaporation (fig. S2), followed by electron beam evaporation of a 50-nm-thick SiO_2 layer to passivate metal electrodes. By using ultrahigh-resolution electron beam lithography (see Materials and Methods) (*32*), we adopted a DesignCAD file with a 5-nm-width dash line to open a window precursor in a spin-cast layer of polymethylmethacrylate. An indented nanogap array (fig. S3) was subsequently formed on the graphene layer between two adjacent gold electrodes by using oxygen plasma etching, resulting in graphene open circuits with carboxylic acid–terminated graphene point contacts (Fig. 1A) that were applied as the platform for the following SMJ investigations. To provide single-molecule functional units, a rigid and conjugated organic strut incorporating bis-*p*-phenylene[34]crown-10 (BPP34C10) and two terminal amine handles, namely, BPP34C10DAM, was designed and synthesized (scheme S1). This functional component was subsequently used to bridge nanogapped graphene point contacts (Fig. 1B) by covalently linking the amino substituents on BPP34C10DAM with carboxylic groups on the edges of graphene sheets using a 1-ethyl-3-(3-dimethylaminopropyl)carbodiimide (EDCI) coupling protocol. The successful establishment of BPP34C10-SMJs was indicated by the resurgence of electrical current (Fig. 1D, red curve). We finally prepared graphene open circuits with appropriate nanogaps, which spatially match the linear backbone length of BPP34C10 host molecules, by optimizing the device fabrication conditions, such as the exposure dose of electron beam and the etching time of oxygen plasma. The optimized results showed that the BPP34C10 connection yield was raised to ~25%, that is, 17 of 68 devices on the same silicon chip showed increased conductance. Moreover, statistical analysis (section S5) confirmed that charge transport through the junction was mainly sustained by an SMJ.

To gain an initial understanding of the effect of host-guest interactions on the conductivity of molecular junctions, we initiated complexation by introducing methyl viologen (MV^{2+}), a well-studied guest for the BPP34C10 host, into the CEM-SMJ system. After immersion in a Me_2SO solution containing 1 mM $MV{\cdot}2PF_6$ for 12 hours, the resulting devices ($MV^{2+}\subset$BPP34C10-SMJ) (Fig. 1C) were rinsed, dried, and tested in the solid state (see Materials and Methods). The electrical currents passing through the SMJs (figs. S4 and S5) showed approximately a one order of magnitude increase on average. The conductance enhancement can be attributed to the host-guest complexation between the MV^{2+} cation and the BPP34C10 host present in the SMJ, forming a $MV^{2+}\subset$BPP34C10 pseudorotaxane.

Real-time electrical measurement

With a temperature-controlling module and a polydimethylsiloxane (PDMS) solvent reservoir (Fig. 2A), the characterization of SMJs at the graphene-liquid interface was performed. Time-dependent electrical characterization was carried out, whereas BPP34C10-SMJs were immersed in a Me_2SO solution containing 1 mM $MV{\cdot}2PF_6$ at 298 K. In general, the current-time (*I-t*) curves obtained (Fig. 2, B and C) show a series of irregular large-amplitude current spikes, which were not observed in the solid-state characterization (figs. S4 and S5). The resulting current-count histogram (Fig. 2D) reveals a bimodal distribution centered at 0.36 and 0.24 nA, respectively, indicating the existence of two distinct "high" and "low" states in $MV^{2+}\subset$BPP34C10-SMJs. In combination with the observation of a change in conductance in the solid state after MV^{2+} addition (Fig. 1D), these results strongly suggest that the current fluctuations between the two distinct levels are related to the association and dissociation processes between the BPP34C10 host and MV^{2+} guest molecules at the device-liquid interface.

To rule out potential artifacts, we established another two kinds of charge transport pathways using (i) a control molecule [oligo(1,4-phenylene ethynylene)diamine (OPEDAM) (*40*)] corresponding to the conjugated backbone of BPP34C10DAM (fig. S6), and (ii) a partially cleaved graphene ribbon device (fig. S7) showing current levels of the same order of magnitude as that of the BPP34C10-SMJ device. *I-t* curves of both devices were recorded (figs. S7 and S8) under the same experimental conditions. In these control experiments, neither of the current-count histograms (figs. S7F and S8F) shows the bimodal distribution characteristics of $MV^{2+}\subset$BPP34C10-SMJs, thus excluding the possibilities of either graphene-MV^{2+} or conjugated backbone-MV^{2+} interactions being the source of the observed electrical spikes.

To gain a better understanding of the correlation between the current flip-flops and host-guest interactions in $MV^{2+}\subset$BPP34C10-SMJs, we calculated the transmission spectra of both the BPP34C10 host and the $MV^{2+}\subset$BPP34C10 pseudorotaxane in the SMJ by using an equilibrium Green's function technique based on density functional theory (DFT), as implemented in the Atomistix ToolKit (ATK) package (see Materials and Methods) (*41*–*43*). The molecular geometries used in the theoretical calculations were based on x-ray crystallographic data taken from the literature (*44*, *45*). In particular, the relative location of the MV^{2+} dication inside the BPP34C10 host was selected for condensed state computations. For the molecular electronic devices, as depicted in Fig. 3 (A and B), the nearest transmission peaks on each side of the Fermi level correspond well to the highest occupied molecular orbital (HOMO) and lowest unoccupied molecular orbital (LUMO) of BPP34C10 and $MV^{2+}\subset$BPP34C10, respectively. In contrast with gold-thiol SMJs (*4*) in which hole transport mainly occurs in the HOMO, in this particular graphene-based system, the perturbed LUMOs dominate the carrier transport behavior because they are near the Fermi level. The calculated transmission spectra of BPP34C10-SMJs and $MV^{2+}\subset$BPP34C10-SMJs are different near the Fermi level. The LUMO transmission peak of the $MV^{2+}\subset$BPP34C10 complex is ~1.93 times larger than that of BPP34C10 ($T_{MV^{2+}\subset BPP34C10}$ = 0.29, $T_{BPP34C10}$ = 0.15), thus leading to a higher conductance. These calculations are consistent with the experimental differential conductivity (dI/dV) curves shown in fig. S5 (C and D). In addition, the effective masses of electrons (LUMO) and holes (HOMO) for BPP34C10 and $MV^{2+}\subset$BPP34C10 were estimated by using the local density approximation (LDA) functional and $1 \times 1 \times 10$ *k*-mesh (see Materials and Methods). These two systems were separately introduced into a periodic cell along the *z* direction to obtain their band structures. For BPP34C10, the effective masses of electrons and holes were 0.81 and 2.93 m_e ($m_e = 9.11 \times 10^{-31}$ kg), respectively. These values, 0.52 and 1.55 m_e for electrons and holes, respectively, were smaller in $MV^{2+}\subset$BPP34C10. The results demonstrate that the mass of electrons is lighter than that of holes, thus once again proving that electron (LUMO) transport is predominant for both BPP34C10 and the $MV^{2+}\subset$BPP34C10 complex in the graphene-based system. The results are also consistent with the molecular projected self-consistent Hamiltonian (MPSH) spectra (Fig. 3, C and D) (*46*), in which the LUMO of the $MV^{2+}\subset$BPP34C10 pseudorotaxane SMJ is more delocalized, providing a better conductive channel. These theoretical calculations shed light on the notable current differences observed during both solid-state and device-liquid interface measurements.

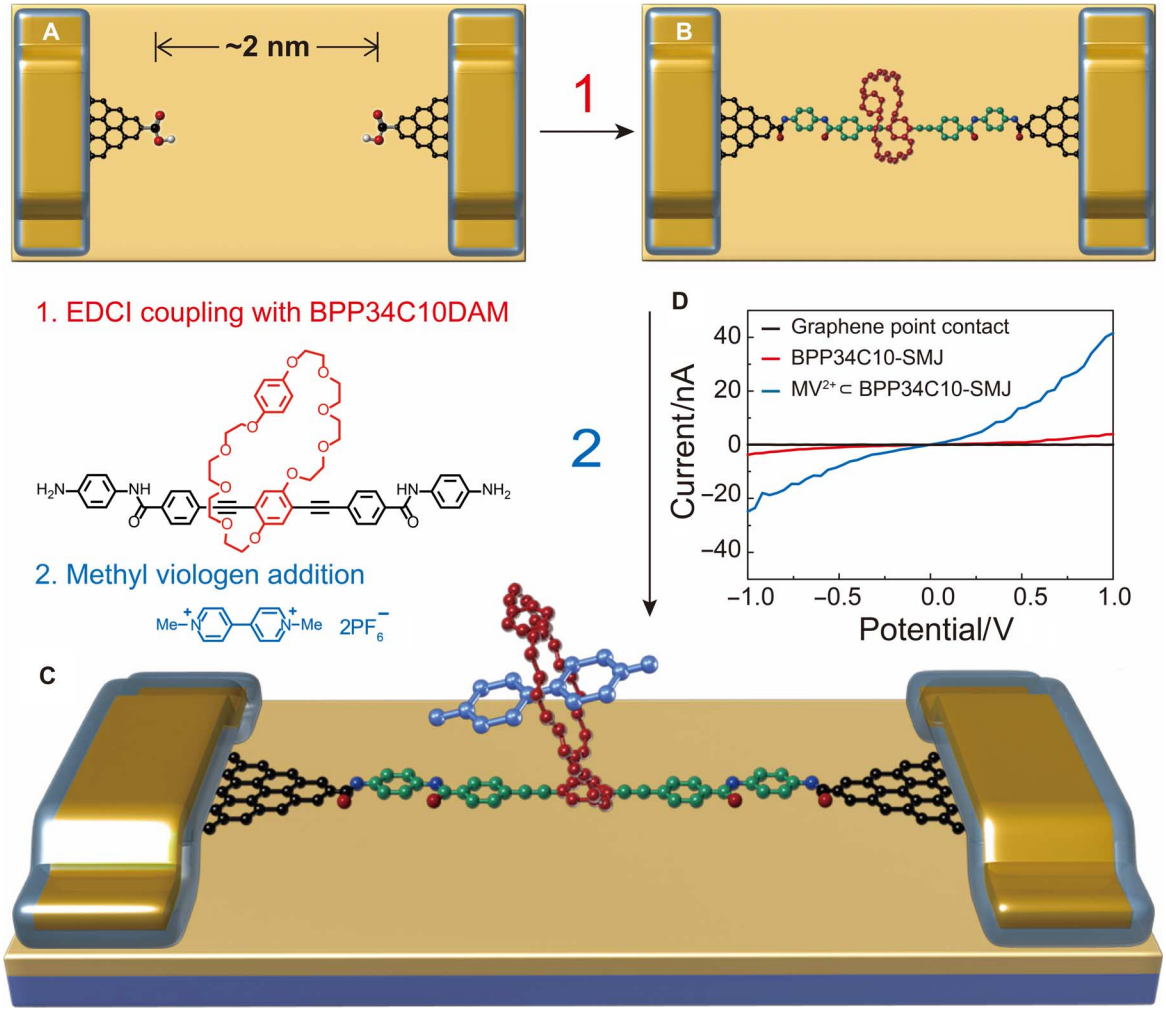

Fig. 1. Fabrication and electrical characterization of SMJ devices. (**A**) Schematic representation of graphene point contacts. The carboxylic acid–terminated graphene point contact arrays were formed with ~2-nm gaps during the dash-line lithographic process. (**B**) Schematic representation of the BPP34C10-SMJ. After treatment with BPP34C10DAM solution in the presence of EDCI coupling reagent, the BPP34C10-SMJ was formed by bridging the conjugated molecular wire across graphene point contacts. (**C**) Schematic representation of the MV^{2+}⊂BPP34C10-SMJ. The BPP34C10-SMJs were treated with MV to form MV^{2+}⊂BPP34C10-SMJ by immersing BPP34C10-SMJ in an MV·$2PF_6$ Me_2SO solution for 12 hours (light brown, SiO_2 substrate; blue, silicon substrate and electrode protection layers; gold, gold electrode). (**D**) Current-voltage (*I-V*) curves of graphene point contacts (black), BPP34C10-SMJ (red), and MV^{2+}⊂BPP34C10-SMJ (blue) in the solid state. The black curve shows that no current occurs after etching; enhanced current (red curve) indicates a successful single-molecule connection; a further increase in current (blue curve) was observed after the addition of MV·$2PF_6$.

Temperature- and solvent-dependent measurements

To investigate the current fluctuations in the MV^{2+}⊂BPP34C10-SMJ system, we recorded the *I-t* curves of BPP34C10-SMJ devices immersed in the Me_2SO solution containing 1 mM MV·$2PF_6$ (see Materials and Methods) at six different temperatures between 273 and 323 K. Similar current spikes and bimodal distributions were observed (Fig. 4, A and B) at each temperature, except for those at 323 K. With the increase in temperature, the current count distributions between the high states (blue curves) and low states (red curves) change gradually. The high states decrease progressively and disappear at 323 K, resulting in an *I-t* curve (Fig. 4A, top) dominated by the flicker (1/*f*) noise. This phenomenon was reproducible (figs. S9 and S10, and section S7) in five different SMJ devices. Considering the fact that the MV^{2+}⊂BPP34C10 complex is less stable at higher temperature as a result of the increased thermal energy (*47*), it is reasonable to relate the low and high current levels to the uncomplexed (free) host (Fig. 3E) and the complexed pseudorotaxane (Fig. 3F) in the MV^{2+}⊂BPP34C10-SMJ, respectively.

Because solvents play important roles in host-guest interactions (*48*), the same experiments were repeated in an aqueous solution of 1 mM MV·2Cl, and *I-t* curves for the MV^{2+}⊂BPP34C10-SMJ devices were recorded at six different temperatures. The results of these measurements (Fig. 4, C and D, and figs. S11 and S12) show similar bimodal distributions and temperature dependences to those obtained in Me_2SO, demonstrating the reproducibility and reliability of the SMJ platform as well as validating the relationship between the low and high states and SMJ configurations.

Thermodynamic analysis

In a two-state model where the BPP34C10 host is either free or complexed with MV^{2+} in the SMJ system, the binding constants (K_a) can be derived from the Langmuir isotherm $K_a = \alpha/(1 - \alpha)C$ (*49*), where α

is the fraction of the BPP34C10 host complexed with MV^{2+}, and C is the concentration of the MV^{2+} dications. On the basis of the Gaussian fits of the *I-t* measurement histograms (Fig. 4, B and D), the integrals of the high- and low-conductance states (A_{high} and A_{low}) were obtained to calculate α and the corresponding K_a values at different temperatures (Table 1 and tables S1 to S6). Other thermodynamic parameters, such as the Gibbs free energy (ΔG^o), the enthalpy (ΔH^o), and the entropy (ΔS^o) for the complexation process between MV^{2+} and BPP34C10 in the $MV^{2+}\subset$BPP34C10-SMJ (Fig. 5A, fig. S13, and Table 1), were deduced by using the van't Hoff equation, $-RT\ln(K_a) = \Delta H^o - T\Delta S^o$

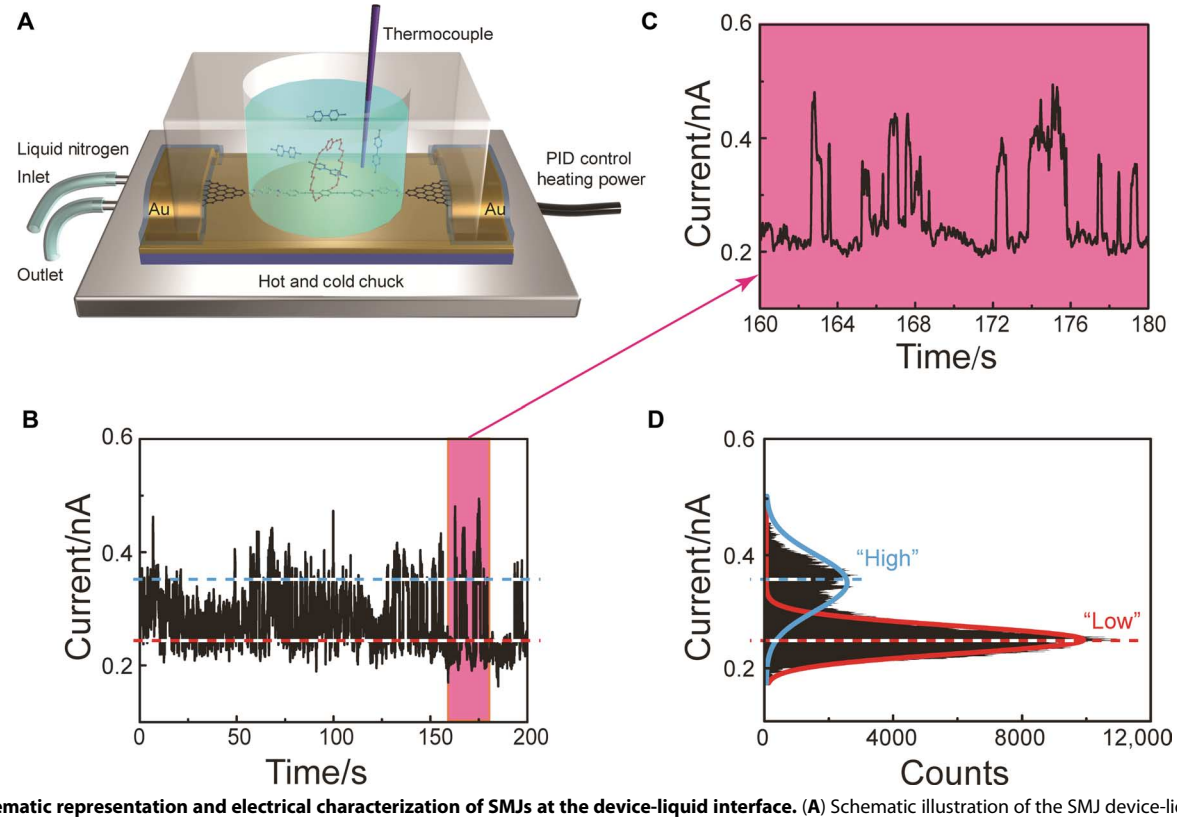

Fig. 2. Schematic representation and electrical characterization of SMJs at the device-liquid interface. (**A**) Schematic illustration of the SMJ device-liquid interface characterization platform. The SMJ device was set onto a hot and cold chuck (silver) and further loaded with a PDMS reservoir (transparent). PID, proportion-integration-differentiation. (**B**) *I-t* curve of BPP34C10-SMJ immersed in a Me_2SO solution of 1 mM MV·$2PF_6$ at room temperature for 200 s with a sampling rate of 28.8 kSa/s. (**C**) Partial *I-t* curve of (B) (160 to 180 s). (**D**) Histogram of (B), showing a bimodal current distribution (V_{bias} = 100 mV).

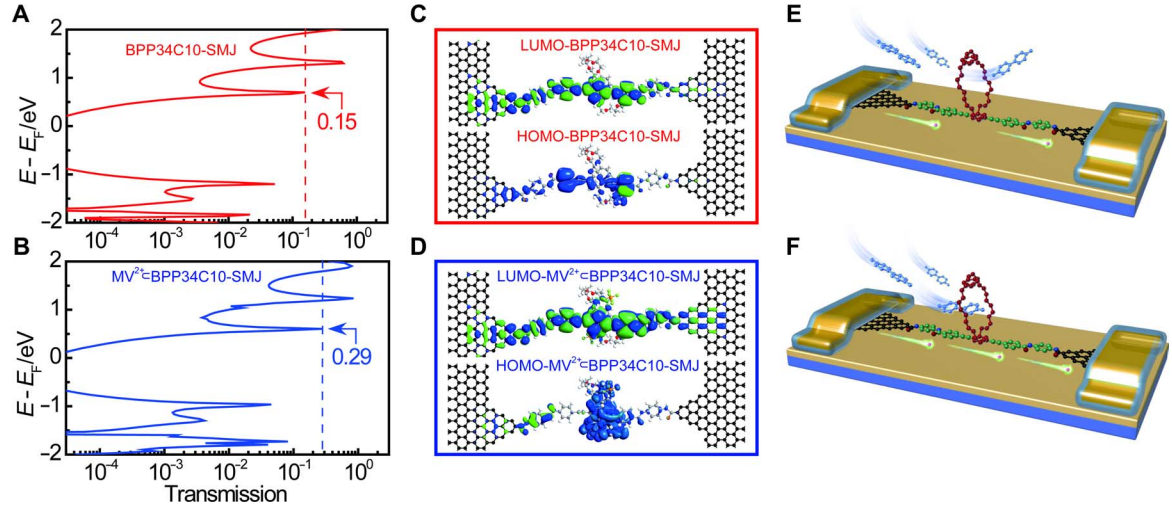

Fig. 3. Computational analyses on BPP34C10 and $MV^{2+}\subset$BPP34C10 between graphene electrodes. (**A** and **B**) Transmission spectra at the equilibrium of BPP34C10 (red) and $MV^{2+}\subset$BPP34C10 (blue) around the Fermi level of graphene electrodes. (**C** and **D**) Diagrams of MPSH HOMO (below) and LUMO (above) of BPP34C10 macrocycle and $MV^{2+}\subset$BPP34C10 pseudorotaxane connected to two graphene electrodes via amide bonds. (**E** and **F**) Schematic representations of charge carriers passing through BPP34C10-SMJ, which is less conductive, and $MV^{2+}\subset$BPP34C10-SMJ, which is more conductive, according to the computational analyses.

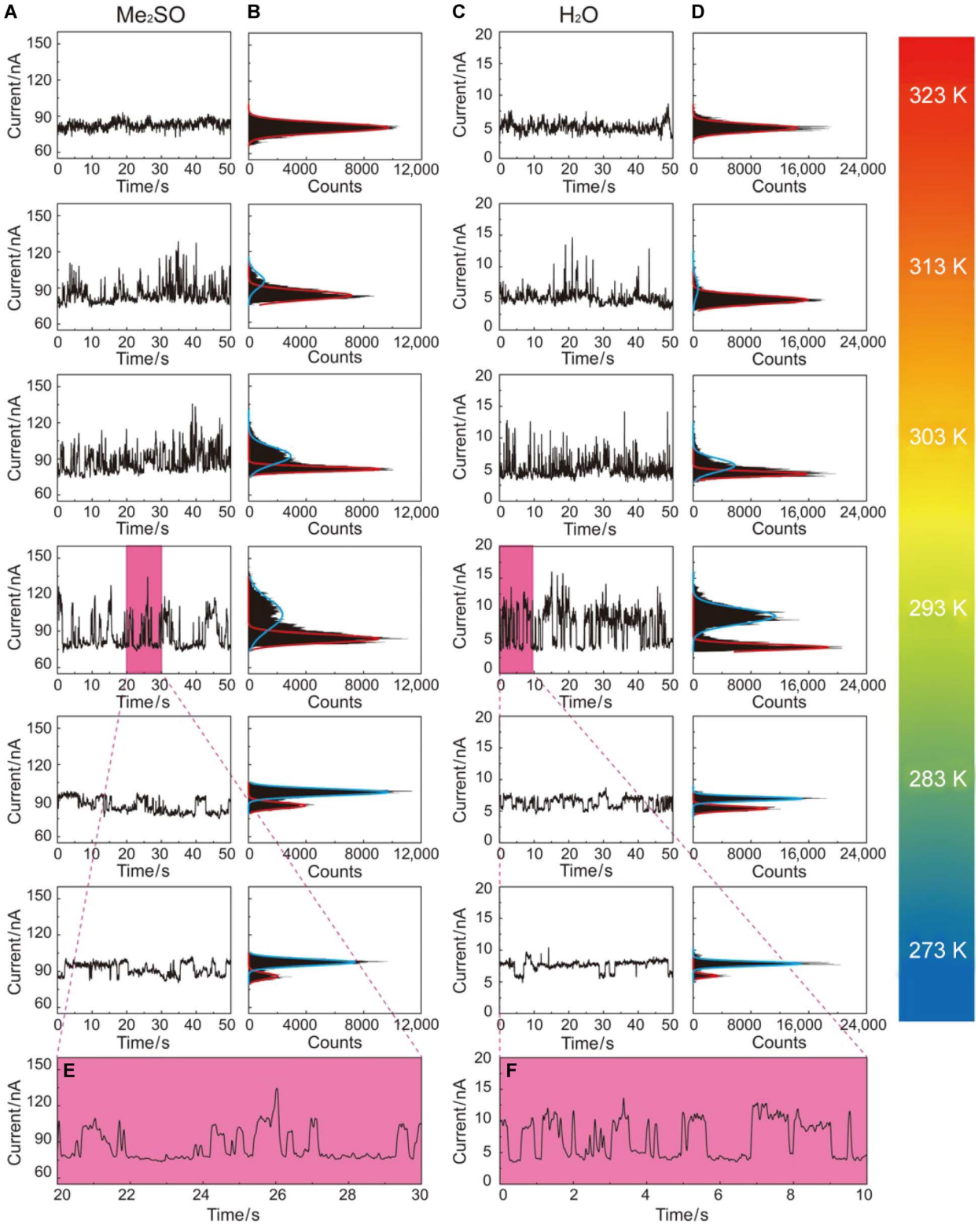

Fig. 4. Real-time measurements of host-guest dynamics in SMJs at the device-liquid interface. (**A**) *I-t* curves and (**B**) the corresponding histograms of a BPP34C10-SMJ device immersed in a 1 mM MV·2PF$_6$ Me_2SO solution at six different temperatures (273 to 323 K) with a sampling rate of 28.8 kSa/s. (**C**) *I-t* curves and (**D**) the corresponding histograms of the same set of devices immersed in a 1 mM MV·2Cl aqueous solution at six different temperatures with a sampling rate of 28.8 kSa/s. In both Me_2SO and aqueous environments, the electric currents passing through SMJs show bimodal distributions from 273 to 313 K. Binding constants (K_a), based on the Langmuir isotherm, can be derived from the current count distributions between two current levels, which change gradually at different temperatures. (**E** and **F**) Partial *I-t* curves (10 s) recorded in Me_2SO and aqueous solutions at 293 K.

Table 1. Thermodynamic parameters for the complex of MV^{2+} with BPP34C10. Thermodynamic data of MV^{2+}⊂BPP34C10 for SMJ device-liquid interface measurements and ^{1}H NMR titrations. N/A, not available.

Solvent	Method	K_a (M^{-1})						ΔG° (kJ mol^{-1})	ΔH° (kJ mol^{-1})	ΔS° (J K^{-1} mol^{-1})	E_a (kJ mol^{-1})	E_d (kJ mol^{-1})
		323 K	313 K	303 K	293 K	283 K	273 K					
Me_2SO	SMJ	N/A	352	717	854	1666	3501	−15.7	−39	−80	−38.7	31.5
	^{1}H NMR	1.7	3.1	6.2	14.4	N/A	N/A	−3.9	−56	−169	N/A	N/A
H_2O	SMJ	N/A	370	858	1572	2515	4786	−17.3	−44	−90	−46.1	38.5
	^{1}H NMR	34.1	37.1	44.5	46.1	N/A	N/A	−9.4	−8.5	−3	N/A	N/A

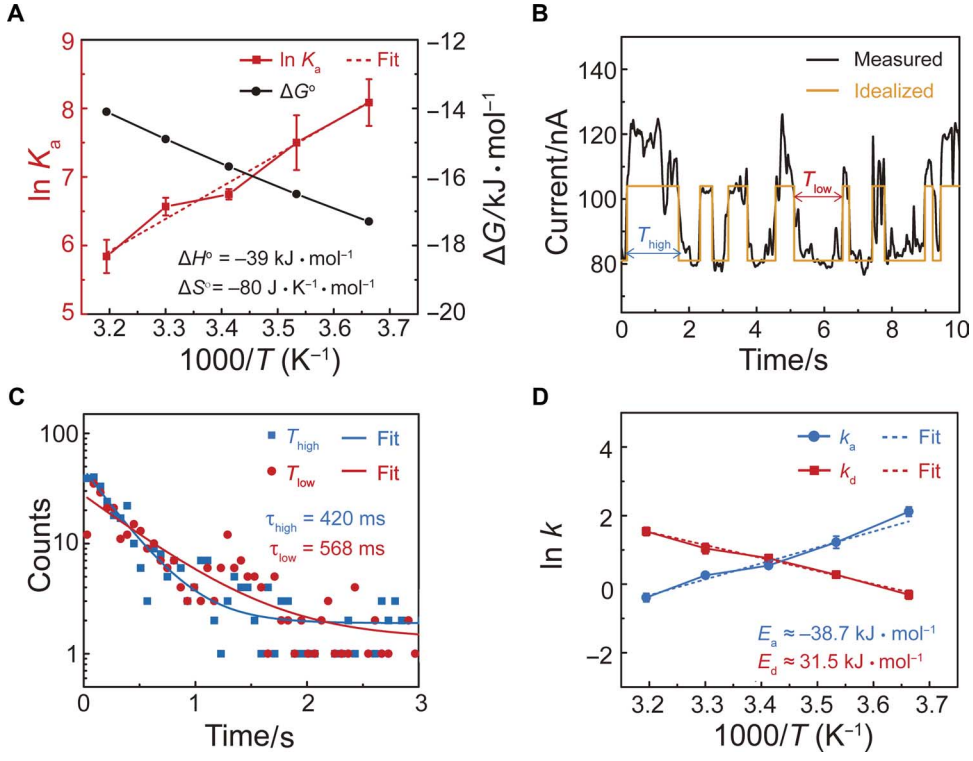

Fig. 5. Thermodynamic and kinetic analyses of the MV^{2+}⊂BPP34C10 complex (de)formation in SMJs at the graphene-liquid interface. (**A**) Plots of the thermodynamic parameters (ln K_a versus 1000/T and ΔG° versus 1000/T) deduced from single-molecule measurements at the SMJ device-Me_2SO interfaces at 293 K. Error bars were calculated from the data obtained from five different devices. ΔH° and ΔS° were obtained by using the van't Hoff equation. (**B**) *I-t* curve (black) of a BPP34C10-SMJ device in a Me_2SO solution of 1 mM MV·2PF_6 at 293 K, and the idealized fit (orange) obtained from segmental *k*-means method based on hidden Markov model analysis using a QUB software (V_{bias} = 100 mV). (**C**) Plots of time intervals of the high (T_{high}, blue) and low (T_{low}, red) current states in the idealized fit in (B), and their exponential fits in which the lifetimes of two states (τ_{high} and τ_{low}) can be derived. (**D**) Arrhenius plots of association ($k_a = 1/\tau_{low}$) and dissociation ($k_d = 1/\tau_{high}$) rate constants deduced (E_a = −38.7 kJ mol^{-1} and E_d = 31.5 kJ mol^{-1}).

(R is ideal gas constant and T is the temperature). It was found that the ΔH° value in Me_2SO is smaller than that in water, whereas the ΔS° value in Me_2SO is larger, thus leading to a more negative value of ΔG° in water, an observation implying that the formation of the MV^{2+}⊂BPP34C10 pseudorotaxane is more spontaneous and stable in an aqueous environment. To compare the K_a values obtained using the SMJ devices with the ensemble thermodynamic data for the BPP34C10-MV^{2+} host-guest system, we performed ^{1}H NMR titration experiments in CD_3SOCD_3 and D_2O at four different temperatures between 293 and 323 K, as shown in fig. S14 and tables S7 and S8. The derived K_a and ΔG° values are listed in Table 1. In the case of the other thermodynamic parameters (Table 1) and in line with the thermodynamic analyses for the graphene SMJ devices, ΔG° was derived from the K_a value, whereas ΔH° and ΔS° were obtained by a linear fitting of the van't Hoff equation, as shown in fig. S15. The negative values obtained for both ΔH° and ΔS° from the ^{1}H NMR titration data indicate that the complexation of BPP34C10 with MV^{2+} in solution is enthalpically driven in both CD_3SOCD_3 and D_2O. Note that Table 1 shows the relatively larger values of K_a and ΔG°, as well as the smaller values of ΔH° and ΔS° in the SMJ system. These differences

can be attributed to the presence of graphene electrodes, which might improve the efficiency of host-guest interactions. Nevertheless, the changing trends of the thermodynamic parameters obtained from the ^{1}H NMR experiments are consistent with the thermodynamic data (Fig. 5A and fig. S15) obtained from the SMJ system, which also implicates an enthalpically driven complexation between BPP34C10 and MV^{2+}, where the host-guest binding is spontaneous at low temperatures, but whose affinity decreases gradually with increasing temperature.

Kinetic analysis

To investigate the relationships between the high- and low-conductance states and the noncovalent bonding interactions in the $MV^{2+}\subset$BPP34C10-SMJ, the *I-t* data were processed initially using a QUB software (Fig. 5B, figs. S16 to S19, and Materials and Methods) (*50*). These idealized two-level flip-flops were analyzed to provide one set of kinetic parameters for the $MV^{2+}\subset$BPP34C10-SMJ devices, including the high and low current lifetimes τ_{high} and τ_{low} (Fig. 5C and figs. S16 to S19), and the corresponding (de)complexation rate constants $k_a = 1/\tau_{low}$ and $k_d = 1/\tau_{high}$ (tables S9 to S14), at different temperatures in both Me_2SO and aqueous solutions. The dwell time histograms (Fig. 5C) show that most time intervals in between blocking events are at the subsecond level. Considering the architecture of the SMJ device, in which a single BPP34C10DAM molecular wire is attached between the graphene point contacts as the charge transport pathway, the reversible on-site (de)complexation processes are presumably first-order. In the case of our results, the high- and low-state time intervals are best fitted as a first-order decaying exponential, suggesting that both states are related to a first-order process in the $MV^{2+}\subset$BPP34C10-SMJ device. In combination with the variations in both the thermodynamic and kinetic parameters at different temperatures (tables S1 to S14), we have been able to confirm that the two-level current fluctuations result from the pseudorotaxane (de)formation processes. The Arrhenius plots of temperature-dependent ln(k) in Me_2SO and H_2O (Fig. 5D and fig. S20) demonstrate a linear dependence between ln(k) and 1000/T, from which the activation energies E_a and E_d of the (de)complexation processes can be derived by using the Arrhenius equation (E_a = −38.7 kJ mol^{-1} and E_d = 31.5 kJ mol^{-1} in Me_2SO; E_a = −46.1 kJ mol^{-1} and E_d = 38.5 kJ mol^{-1} in H_2O). The E_a in Me_2SO is higher than that in water, whereas the E_d in Me_2SO is lower, showing that BPP34C10 has a higher affinity for MV^{2+} in H_2O, an observation that is consistent with the thermodynamic analysis and previous ensemble experiments (*51*). Note that the values of E_a are negative. This observation is not unreasonable, given the fact that the host-guest reaction is generally known to be a barrier-less elementary reaction, where the reaction relies on the capture of the molecules in a potential well. In the present case, increasing the temperature leads to a reduced probability of the colliding crown ether host capturing the MV^{2+} dicationic guest. Therefore, the reaction rates decrease with increasing temperature, resulting in a negative value for E_a.

CONCLUSION

In conclusion, we have demonstrated a new and reliable single-molecule electrical approach in which molecular electronics is interfaced with an analytical system to probe the dynamic behavior of a host-guest complex with high time resolution in a nondestructive manner. We are firmly of the opinion that this SMJ platform is ready to be applied immediately to a variety of label-free single-molecule chemodetections/biodetections, such as DNA mutation, protein folding, enzymatic activity, and DNA sequencing. In addition, with proven reliability and compatibility with current microelectronic fabrication technologies, graphene-molecule SMJs hold a great deal of promise for the development of low-noise multiplex detection electronics for accurate molecular and point-of-care clinical diagnosis.

MATERIALS AND METHODS

Device fabrication and molecular connection

The devices with graphene point contact arrays were fabricated by a dash-line lithographic method described in the Supplementary Materials. Note that a 50-nm-thick SiO_2 layer (the light brown part of graphene devices in Fig. 1) was deposited by e-beam thermal evaporation following resistance thermal deposition of patterned metallic electrodes (8 nm/60 nm, Cr/Au). The SiO_2 passivation layers on gold electrode surfaces prevented any direct contact and leakage between the solution and the metal electrodes during the subsequent electrical measurements in Me_2SO or aqueous solutions.

After the lithographic process, the freshly prepared graphene point contact array devices (five sets in total) were immersed in a pyridine solution with 0.1 mM BPP34C10DAM when carrying out coupling reactions with 1 mM EDCI. After leaving them to react for 48 hours, the devices were removed from the solution, rinsed with deionized H_2O and Me_2CO several times, and then dried with a N_2 stream. The as-prepared SMJ devices were ready for solid-state characterization and the addition of MV salts. For $MV{\cdot}2PF_6$ addition, the BPP34C10-SMJ devices were immersed in a Me_2SO solution of 1 mM $MV{\cdot}2PF_6$ for 12 hours. The devices were removed from solution, rinsed with deionized H_2O and Me_2CO, and then dried with a N_2 stream before electrical characterization.

Electrical characterization

The solid-state electrical characterization (*I-V* and *I-t*) was carried out carefully at room temperature in the ambient atmosphere using an Agilent 4155C semiconductor parameter system [direct current (DC) measurements] and a Karl Suss (PM5) manual probe station. The single-molecule dynamics in Me_2SO and aqueous solutions was monitored with a ziControl program. The electrical current through selected electrode pairs was monitored using a transimpedance current amplifier (HF2LI lock-in amplifier) at a sampling rate of 28.8 kSa/s by a NIDAQ card, realizing a microsecond time scale. The transimpedance amplifier also set a DC voltage to the source-drain electrodes with a bandwidth filter of 1 kHz (1 to 100 nA/V sensitivity). In general, we used the two-terminal device architecture (without use of the back gate) to characterize the device performance at the voltage bias (V_{bias}) of 100 mV.

Temperature control

The device was fixed on the test stage, which consists of a manual probe station and an INSTEC hot and cold chuck (HCC214S, INSTEC), with a proportion-integration-differentiation control system and a liquid N_2 cooling system, controlling temperature precisely from −120° to 200°C with high-resolution (0.001°C) and ultrahigh-temperature stability (better than ±0.1°C). The proportion-integration-differentiation controller can provide a programmable heating or cooling process with the aid of liquid N_2 and can also be automatically regulated, achieving a constant rate to warm or cool the surface of the chuck. A thermocouple

was used to monitor the temperature of the solvent reservoir. When thermal equilibrium was reached (~15 min) at particular temperatures, the *I-t* curves of the SMJ were recorded.

Theoretical calculations

The geometric optimizations for graphene-based electrode systems of the BPP34C10 host and the MV^{2+}⊂BPP34C10 pseudorotaxane (fig. S21), which mimic the experimental molecular junctions, were performed using the semiempirical method AM1 within the Gaussian 03 package. Once the molecular structure was relaxed, DFT was used to compute the molecular orbitals. The hybrid functional B3LYP with a basis set of 6-31+G* was used. The transmission spectra were calculated within the framework of DFT combined with an equilibrium Green's function method within the ATK package. The local LDA exchange-correlation functional and the double-zeta basis were used. The kinetic energy cutoff was selected to be 100 Ha. The sampling of the Brillouin zone was 10 × 10 × 100 according to the Monkhorst-Pack scheme.

SUPPLEMENTARY MATERIALS

Supplementary material for this article is available at http://advances.sciencemag.org/cgi/content/full/2/11/e1601113/DC1

Supplementary Materials and Methods

scheme S1. Synthesis of BPP34C10DAM from BPP34C10DA.

fig. S1. Schematic representation of the fabrication procedure to form graphene field-effect transistor arrays.

fig. S2. Optical microscopic images of graphene devices with different magnification.

fig. S3. Characterization of an indented nanogap array.

fig. S4. Solid-state electrical characterization.

fig. S5. Reproducibility and differential conductance spectra.

fig. S6. Schematic processes used to fabricate molecular devices.

fig. S7. Control experiments using a partially cleaved graphene ribbon device.

fig. S8. Control experiments using an OPEDAM-connected device.

figs. S9 to S12. Real-time measurements of host-guest dynamics in SMJs at the device-liquid interface.

fig. S13. Thermodynamic analyses of SMJ devices.

fig. S14. ^{1}H NMR titration.

fig. S15. Thermodynamic analyses of SMJ devices.

figs. S16 to S19. Host-guest kinetics analysis.

fig. S20. Host-guest kinetics analysis.

fig. S21. Geometric optimizations of BPP34C10 and MV^{2+}⊂BPP34C10 complexes.

tables S1 to S6. Binding constants.

table S7. Chemical shifts for ^{1}H NMR titrations in CD_3SOCD_3.

table S8. Chemical shifts for ^{1}H NMR titrations in D_2O.

tables S9 to S14. Dissociation (k_d) and association (k_a) rate constants.

REFERENCES AND NOTES

1. A. Aviram, M. A. Ratner, Molecular rectifiers. *Chem. Phys. Lett.* **29**, 277–283 (1974).
2. A. Nitzan, M. A. Ratner, Electron transport in molecular wire junctions. *Science* **300**, 1384–1389 (2003).
3. S. V. Aradhya, L. Venkataraman, Single-molecule junctions beyond electronic transport. *Nat. Nanotechnol.* **8**, 399–410 (2013).
4. L. Sun, Y. A. Diaz-Fernandez, T. A. Gschneidtner, F. Westerlund, S. Lara-Avila, K. Moth-Poulsen, Single-molecule electronics: From chemical design to functional devices. *Chem. Soc. Rev.* **43**, 7378–7411 (2014).
5. R. M. Metzger, Unimolecular electronics. *Chem. Rev.* **115**, 5056–5115 (2015).
6. C. Jia, B. Ma, N. Xin, X. Guo, Carbon electrode–molecule junctions: A reliable platform for molecular electronics. *Acc. Chem. Res.* **48**, 2565–2575 (2015).
7. H. Song, M. A. Reed, T. Lee, Single molecule electronic devices. *Adv. Mater.* **23**, 1583–1608 (2011).
8. F. Schwarz, G. Kastlunger, F. Lissel, C. Egler-Lucas, S. N. Semenov, K. Venkatesan, H. Berke, R. Stadler, E. Lörtscher, Field-induced conductance switching by charge-state alternation in organometallic single-molecule junctions. *Nat. Nanotechnol.* **11**, 170–176 (2016).
9. B. Capozzi, J. Xia, O. Adak, E. J. Dell, Z.-F. Liu, J. C. Taylor, J. B. Neaton, L. M. Campos, L. Venkataraman, Single-molecule diodes with high rectification ratios through environmental control. *Nat. Nanotechnol.* **10**, 522–527 (2015).
10. H. Vazquez, R. Skouta, S. Schneebeli, M. Kamenetska, R. Breslow, L. Venkataraman, M. S. Hybertsen, Probing the conductance superposition law in single-molecule circuits with parallel paths. *Nat. Nanotechnol.* **7**, 663–667 (2012).
11. C. M. Guédon, H. Valkenier, T. Markussen, K. S. Thygesen, J. C. Hummelen, S. J. van der Molen, Observation of quantum interference in molecular charge transport. *Nat. Nanotechnol.* **7**, 305–309 (2012).
12. C. W. Marquardt, S. Grunder, A. Błaszczyk, S. Dehm, F. Hennrich, H. Löhneysen, M. Mayor, R. Krupke, Electroluminescence from a single nanotube-molecule-nanotube junction. *Nat. Nanotechnol.* **5**, 863–867 (2010).
13. Y. Kim, W. Jeong, K. Kim, W. Lee, P. Reddy, Electrostatic control of thermoelectricity in molecular junctions. *Nat. Nanotechnol.* **9**, 881–885 (2014).
14. S. Sanvito, Molecular spintronics. *Chem. Soc. Rev.* **40**, 3336–3355 (2011).
15. X. Guo, Single-molecule electrical biosensors based on single-walled carbon nanotubes. *Adv. Mater.* **25**, 3397–3408 (2013).
16. J. E. Green, J. W. Choi, A. Boukai, Y. Bunimovich, E. Johnston-Halperin, E. Delonno, Y. Luo, B. A. Sheriff, K. Xu, Y. S. Shin, H.-R. Tseng, J. F. Stoddart, J. R. Heath, A 160-kilobit molecular electronic memory patterned at 10^{11} bits per square centimetre. *Nature* **445**, 414–417 (2007).
17. F. Patolsky, G. Zheng, O. Hayden, M. Lakadamyali, X. Zhuang, C. M. Lieber, Electrical detection of single viruses. *Proc. Natl. Acad. Sci. U.S.A.* **101**, 14017–14022 (2004).
18. J. Wang, F. Shen, Z. Wang, G. He, J. Qin, N. Cheng, M. Yao, L. Li, X. Guo, Point decoration of silicon nanowires: An approach toward single-molecule electrical detection. *Angew. Chem. Int. Ed. Engl.* **53**, 5038–5043 (2014).
19. Y. Choi, I. S. Moody, P. C. Sims, S. R. Hunt, B. L. Corso, I. Perez, G. A. Weiss, P. G. Collins, Single-molecule lysozyme dynamics monitored by an electronic circuit. *Science* **335**, 319–324 (2012).
20. S. Sorgenfrei, C.-y. Chiu, R. L. Gonzalez Jr, Y.-J. Yu, P. Kim, C. Nuckolls, K. L. Shepard, Label-free single-molecule detection of DNA-hybridization kinetics with a carbon nanotube field-effect transistor. *Nat. Nanotechnol.* **6**, 126–132 (2011).
21. H. Liu, J. He, J. Tang, H. Liu, P. Pang, D. Cao, P. Krstic, S. Joseph, S. Lindsay, C. Nuckolls, Translocation of single-stranded DNA through single-walled carbon nanotubes. *Science* **327**, 64–67 (2010).
22. T. P. Burg, M. Godin, S. M. Knudsen, W. Shen, G. Carlson, J. S. Foster, K. Babcock, S. R. Manalis, Weighing of biomolecules, single cells and single nanoparticles in fluid. *Nature* **446**, 1066–1069 (2007).
23. S. Howorka, Z. Siwy, Nanopore analytics: Sensing of single molecules. *Chem. Soc. Rev.* **38**, 2360–2384 (2009).
24. Y. Zhao, B. Ashcroft, P. Zhang, H. Liu, S. Sen, W. Song, J. Im, B. Gyarfas, S. Manna, S. Biswas, C. Borges, S. Lindsay, Single-molecule spectroscopy of amino acids and peptides by recognition tunnelling. *Nat. Nanotechnol.* **9**, 466–473 (2014).
25. M. A. Reed, C. Zhou, C. J. Muller, T. P. Burgin, J. M. Tour, Conductance of a molecular junction. *Science* **278**, 252–254 (1997).
26. X. D. Cui, A. Primak, X. Zarate, J. Tomfohr, O. F. Sankey, A. L. Moore, T. A. Moore, D. Gust, G. Harris, S. M. Lindsay, Reproducible measurement of single-molecule conductivity. *Science* **294**, 571–574 (2001).
27. B. Xu, N. J. Tao, Measurement of single-molecule resistance by repeated formation of molecular junctions. *Science* **301**, 1221–1223 (2003).
28. W. Liang, M. P. Shores, M. Bockrath, J. R. Long, H. Park, Kondo resonance in a single-molecule transistor. *Nature* **417**, 725–729 (2002).
29. L. Qin, S. Park, L. Huang, C. A. Mirkin, On-wire lithography. *Science* **309**, 113–115 (2005).
30. T. Li, W. Hu, D. Zhu, Nanogap electrodes. *Adv. Mater.* **22**, 286–300 (2010).
31. A. K. Feldman, M. L. Steigerwald, X. Guo, C. Nuckolls, Molecular electronic devices based on single-walled carbon nanotube electrodes. *Acc. Chem. Res.* **41**, 1731–1741 (2008).
32. Y. Cao, S. Dong, S. Liu, L. He, L. Gan, X. Yu, M. L. Steigerwald, X. Wu, Z. Liu, X. Guo, Building high-throughput molecular junctions using indented graphene point contacts. *Angew. Chem. Int. Ed. Engl.* **51**, 12228–12232 (2012).
33. Y. Cao, S. Dong, S. Liu, Z. Liu, X. Guo, Toward functional molecular devices based on graphene–molecule junctions. *Angew. Chem. Int. Ed. Engl.* **52**, 3906–3910 (2013).
34. F. Gao, W.-J. Ruan, J.-M. Chen, Y.-H. Zhang, Z.-A. Zhu, Spectroscopy, NMR and DFT studies on molecular recognition of crown ether bridged chiral heterotrinuclear salen Zn(II) complex. *Spectrochim. Acta A Mol. Biomol. Spectrosc.* **62**, 886–895 (2005).
35. J. Kalmár, S. B. Ellis, M. T. Ashby, R. L. Halterman, Kinetics of formation of the host-guest complex of a viologen with cucurbit[7]uril. *Org. Lett.* **14**, 3248–3251 (2012).
36. K. Hirose, A practical guide for the determination of binding constants. *J. Incl. Phenom. Macrocycl. Chem.* **39**, 193–209 (2001).
37. A. L. Schmucker, G. Barin, K. A. Brown, M. Rycenga, A. Coskun, O. Buyukcakir, K. D. Osberg, J. F. Stoddart, C. A. Mirkin, Electronic and optical vibrational spectroscopy of molecular transport junctions created by on-wire lithography. *Small* **9**, 1900–1903 (2013).

38. A. G. Palmer III, NMR characterization of the dynamics of biomacromolecules. *Chem. Rev.* **104**, 3623–3640 (2004).
39. P. Thordarson, Determining association constants from titration experiments in supramolecular chemistry. *Chem. Soc. Rev.* **40**, 1305–1323 (2011).
40. M. T. González, X. Zhao, D. Z. Manrique, D. Miguel, E. Leary, M. Gulcur, A. S. Batsanov, G. Rubio-Bollinger, C. J. Lambert, M. R. Bryce, N. Agraït, Structural versus electrical functionalization of oligo(phenyleneethynylene) diamine molecular junctions. *J. Phys. Chem. C* **118**, 21655–21662 (2014).
41. A. D. Becke, Density-functional thermochemistry. III. The role of exact exchange. *J. Chem. Phys.* **98**, 5648–5652 (1993).
42. Y. Imry, R. Landauer, Conductance viewed as transmission. *Rev. Mod. Phys.* **71**, S306–S312 (1999).
43. M. Brandbyge, J.-L. Mozos, P. Ordejón, J. Taylor, K. Stokbro, Density-functional method for nonequilibrium electron transport. *Phys. Rev. B* **65**, 165401 (2002).
44. Y.-L. Zhao, L. Liu, W. Zhang, C.-H. Sue, Q. Li, O. Miljanić, O. M. Yaghi, J. F. Stoddart, Rigid-strut-containing crown ethers and [2]catenanes for incorporation into metal–organic frameworks. *Chem. Eur. J.* **15**, 13356–13380 (2009).
45. Q. Li, W. Zhang, O. Miljanić, C.-H. Sue, Y.-L. Zhao, L. Liu, C. B. Knobler, J. F. Stoddart, O. M. Yaghi, Docking in metal-organic frameworks. *Science* **325**, 855–859 (2009).
46. J. Taylor, H. Guo, J. Wang, *Ab initio* modeling of quantum transport properties of molecular electronic devices. *Phys. Rev. B* **63**, 245407 (2001).
47. H.-J. Schneider, Mechanisms of molecular recognition: Investigations of organic host–guest complexes. *Angew. Chem. Int. Ed.* **30**, 1417–1436 (1991).
48. T. Douglas, M. Young, Host-guest encapsulation of materials by assembled virus protein cages. *Nature* **393**, 152–155 (1998).
49. P. Gong, R. Levicky, DNA surface hybridization regimes. *Proc. Natl. Acad. Sci. U.S.A.* **105**, 5301–5306 (2008).
50. L. S. Milescu, A. Yildiz, P. R. Selvin, F. Sachs, Maximum likelihood estimation of molecular motor kinetics from staircase dwell-time sequences. *Biophys. J.* **91**, 1156–1168 (2006).
51. B. L. Allwood, N. Spencer, H. Shahriari-Zavareh, J. F. Stoddart, D. J. Williams, Complexation of paraquat by a bisparaphenylene-34-crown-10 derivative. *J. Chem. Soc. Chem. Commun.* 1064–1066 (1987).

Acknowledgments

Funding: We acknowledge primary financial supports from the 973 National Basic Research Program of China (2012CB921404 and 2015CB856500) (to X.G., A.C.-H.S., J.F.S., and M.A.O.), the National Natural Science Foundation of China (21225311, 51121091, 91333102, and 21373014) (to X.G. and L.L.), the China Postdoctoral Science Foundation (2014M550548) (to H.W.), the National Thousand Talents Program Plan B of China (to J.F.S.), and the National Thousand Young Talents Program of China (to M.A.O. and A.C.-H.S.). **Author contributions:** X.G., A.C.-H.S., and J.F.S. conceived and designed the experiments. H.W., J.C., and G.H. performed the device fabrication and electrical measurements. W.L. and M.A.O. carried out the molecular synthesis and ^{1}H NMR spectroscopy. L.L. performed the theoretical calculation. X.G., A.C.-H.S., J.F.S., H.W., and W.L. analyzed the data and wrote the paper. All the authors discussed the results and commented on the manuscript. **Competing interests:** The authors declare that they have no competing interests. **Data and materials availability:** All data needed to evaluate the conclusions in the paper are present in the paper and/or the Supplementary Materials. Additional data related to this paper may be requested from the authors.

Submitted 17 May 2016
Accepted 21 October 2016
Published 25 November 2016
10.1126/sciadv.1601113

Citation: H. Wen, W. Li, J. Chen, G. He, L. Li, M. A. Olson, A. C.-H. Sue, J. F. Stoddart, X. Guo, Complex formation dynamics in a single-molecule electronic device. *Sci. Adv.* **2**, e1601113 (2016).